JOURNAL OF THERMOPHYSICS AND HEAT TRANSFER
Vol. 15, No. 2, April–June 2001

Predictions of Ablating Hypersonic Vehicles Using an Iterative Coupled Fluid/Thermal Approach

David W. Kuntz,* Basil Hassan,† and Donald L. Potter‡
Sandia National Laboratories, Albuquerque, New Mexico 87185

A new iterative approach for the prediction of the ablation of hypersonic vehicles is presented. The solution technique is achieved by an iterative coupling of a computational fluid dynamics code and a material thermal response code through mass and energy balances at a common interface. The iterative approach proved necessary due to severe numerical instabilities that resulted when an explicit technique was employed involving a loose coupling approach between the two codes. The results presented are for an axisymmetric carbon–carbon nosetip on a reentry vehicle flying a ballistic trajectory. Details of the computational technique and the computed flowfield and material thermal response are presented. Comparisons were made with the widely used ABRES Shape Change Code (ASCC), and favorable results were obtained.

Nomenclature

A_s, B_s, C_s	=	coefficients used in the Blottner et al.[37] viscosity formula
B'_c	=	dimensionless ablation mass transfer
C	=	Arrhenius rate preexponential coefficient
C_h	=	convective heat transfer coefficient, kg/s · m^2
C_m	=	convective mass transfer coefficient, kg/s · m^2
C_p	=	material specific heat, J/kg · K
c_{ij}	=	coefficients in the solid mechanics formulation
i	=	enthalpy, J/kg
k	=	thermal conductivity of solid, W/m · K
k_f	=	forward reaction rate, cm^3/mol · s
$\dot{m}''_c$	=	mass loss rate per unit area, kg/s · m^2
n	=	normal coordinate, m
$\hat{n}$	=	unit vector normal (inward) to the ablating surface
n_x, n_y	=	x and y components of the unit normal vector
P	=	pressure, Pa
Q^*	=	heat of ablation, J/kg
q_{conv}	=	convective heat transfer rate, W/m^2
$\dot{s}$	=	surface recession rate, m/s
T	=	translational/rotational temperature, K
T_d	=	characteristic temperature of dissociation, K
T_{ve}	=	vibrational/electronic temperature, K
x, y, z	=	Cartesian coordinates, m
Δt	=	time step, s
δx	=	nodal displacement in the x direction, m
δy	=	nodal displacement in the y direction, m
ε	=	surface emittance
η	=	Arrhenius rate temperature coefficient
μ	=	viscosity, kg/m · s
ρ	=	density (gas or solid), kg/m^3
σ	=	Stefan–Boltzmann constant, 5.6697×10^8 W/m^2 · K^4

Subscripts

c	=	char property
n	=	surface nodal property
r	=	recovery property
ref	=	reference property
s	=	species
w	=	wall property
∞	=	surroundings

Introduction

ABLATING thermal protection systems are commonly used to protect the structures of reentering hypersonic vehicles in severe heating environments. Numerical prediction of ablation is challenging due to the complex multiphase physical and chemical processes that occur. A coupled approach is necessary in situations in which shape change is significant and, thus, has a significant effect on aerodynamics and heating rates. Computational coupling between high-temperature fluid dynamics and material thermal response has taken many forms. The most widely used numerical approach in the U.S. aerospace industry for predicting ablation was developed by the Aerotherm Corporation in the late 1960s.[1–6] The technique involved using a boundary layer approach (BLIMP code)[3] for the fluid dynamics and a one-dimensional in-depth heat conduction and charring response procedure (CMA code)[2] for the material thermal response. The main restrictions of the inviscid/boundary layer approaches for the fluid computations are a result of the boundary layer assumptions and the application to relatively simple shapes and flowfields. Later work has used coupled inviscid/viscous flow techniques, like viscous shock layer,[7,8] parabolized Navier–Stokes,[9] and full Navier–Stokes,[10–18] to alleviate some of the preceding assumptions and allow for more complex vehicles to be analyzed.

With improvements in computational algorithms and advances in computer hardware, Navier–Stokes based approaches have become the norm in recent years for coupling to material thermal response predictions. Conti et al.[10] made an early attempt to couple Navier–Stokes calculations to the material thermal response for axisymmetric reentry flowfields. The surface temperatures and ablation rates were computed based on an interface surface energy balance, with conduction within the material only occurring in the direction normal to the surface. The flowfield calculations and material response calculations were coupled at every time step using either a quasi-steady approach or a fully transient mode. The chemistry was modeled by a two-species gas model consisting of equilibrium air and a single ablation product, which was not allowed to react with the air as it diffused across the boundary layer. Surface recession and dynamic deformation of the thermal grid were

Received 12 June 2000; revision received 27 September 2000; accepted for publication 2 October 2000.

*Principal Member of Technical Staff, Aerosciences and Compressible Fluid Mechanics Department, P.O. Box 5800, Mail Stop 0825; dwkuntz@sandia.gov. Associate Fellow AIAA.

†Principal Member of Technical Staff, Thermal/Fluid Computational Engineering Sciences Department, P.O. Box 5800, Mail Stop 0835; bhassan@sandia.gov. Associate Fellow AIAA.

‡Senior Member of Technical Staff, Aerosciences and Compressible Fluid Mechanics Department, P.O. Box 5800, Mail Stop 0825; dlpotte@sandia.gov.

allowed during the trajectory, and the fluid mechanics grid was remeshed at the fixed trajectory points to conform to the new surface shape.

Chen and Henline[11] derived a general surface boundary condition for the Navier–Stokes equations considering the surface thermochemistry effects. Surface energy and mass balances were derived for nonequilibrium or equilibrium gas states adjacent to ablating or nonablating surfaces. Chen et al.[12] later applied this approach to coupling an axisymmetric Navier–Stokes code with the one-dimensional, transient, CMA code. Ablation products from mass blowing were allowed to react with a nonequilibrium air flowfield. However, the surface was not recessed. The approach was loosely coupled in an iterative manner until the computational fluid dynamics (CFD) supplied heating rates and the CMA-supplied temperatures and ablation rates produced variations in surface temperature and blowing rates of less than 0.1%. The surface chemistry was computed under equilibrium conditions before the resultant products were allowed to react with the flowfield species. Olynick et al.[13,14] used the same technique, but also coupled it with a flowfield radiation calculation. Bhutta et al.[15] used a similar approach for axisymmetric flows and allowed surface recession.

Keenan and Candler[16,17] coupled the fluid and solid by a surface mass and energy balance that assumed a general thermochemical ablation model that included the effects of chemical nonequilibrium at the surface. The material chosen for the ablator was noncharring. The thermochemical nonequilibrium flowfield calculations were axisymmetric with two-dimensional, heat conduction computed inside the solid. In this investigation, the surface was stationary.

More recent work by Chen and Milos[18] has investigated shape change simulations for charring materials. The governing equations include both energy conservation and a three-component decomposition model with a moving grid. Blowing corrections are applied to the nonablating (cold wall) heat transfer rates in their coupled fluid/thermal simulations.

Recent work by the present authors[19] coupled thermochemical nonequilibrium Navier–Stokes calculations with multidimensional in-depth heat conduction that includes ablation of the surface material with shape change. The algorithm was a loosely coupled, or explicit, approach in which the computed results from the Navier–Stokes solution (heat transfer coefficient, pressure, and recovery enthalpy) were held constant, while the material response code marched in time from one CFD trajectory point calculation to the next, computing the ablation, shape change, and surface and in-depth temperatures. The highly nonlinear nature of the ablation process resulted in severe instabilities in computed heat transfer and ablation rates, particularly late in the trajectory. As a result of this unstable behavior, an iterative technique,[20] similar to approaches developed by Olynick et al.[13,14] and Kontinos,[21] has been developed that eliminates the instabilities associated with the previous technique and results in a significantly more accurate prediction of the ablation process. Details of this iterative technique, including the computed results for a low-angle, sphere–cone nosetip of a hypersonic reentry vehicle, are presented in this paper.

Computational Fluid Dynamics

The CFD calculations are performed using SACCARA. SACCARA is based on PINCA,[22,23] a distributed parallel version of the commercial, finite volume, Navier–Stokes code INCA,[24] from Amtec, Inc. SACCARA solves the two-dimensional/axisymmetric and three-dimensional full Navier–Stokes equations for flows in thermochemical nonequilibrium. The code employs multiblock structured grids and can be run on a variety of shared memory or distributed memory parallel platforms. The solution is driven to a steady state using the lower–upper symmetric Gauss–Seidel (LU-SGS) or diagonal implicit solution advancement scheme based on a combination of the work of Yoon and Jameson,[25] Yoon and Kwak,[26] and Peery and Imlay.[27] The inviscid fluxes are evaluated using the flux vector splitting of Steger and Warming[28] or the symmetric total variation diminishing (TVD) flux function of Yee.[29] The current calculations employ the second-order Steger–Warming[28] flux vector splitting. The viscous terms employ a standard, second-order, central differencing scheme. Previous benchmark validation calculations demonstrating the SACCARA's ability to compute hypersonic flows over sphere–cone geometries with comparison to both flight and ground test data have been documented by Roy and Blottner[30] and Roy et al.[31]

For the high-altitude calculations, the flow is assumed to be in thermochemical nonequilibrium. Equations for conservation of mass of each chemical species, conservation of momentum, conservation of total energy, and conservation of vibrational/electronic energy are solved. These equations are described in a number of sources, including Refs. 32 and 33. For the lower altitude portion of the trajectory, thermal equilibrium is assumed when the thermal nonequilibrium solutions provide nearly identical translational/rotational and vibrational/electronic temperatures. The thermal state is indicated in Table 1, which also details the freestream conditions for the trajectory.

Table 1 Freestream conditions for coupled calculations

Trajectory point	Time, s	Altitude, m	Velocity, m/s	Temp., K	Pressure, Pa	Density, kg/m^3	Mach no.	Thermal state
1	0	66935	6780.6	227.81	8.1757	1.2505×10^{-4}	22.41	TNEQ[a]
2	4.25	55842	6788.3	258.02	37.362	5.0454×10^{-4}	21.08	TNEQ
3	6.75	49290	6785.2	270.65	88.118	1.1344×10^{-3}	20.57	TNEQ
4	8.75	44042	6773.0	261.40	169.50	2.2593×10^{-3}	20.90	TNEQ
5	10.25	40108	6752.4	250.35	287.14	3.9957×10^{-3}	21.29	TNEQ
6	11.50	36836	6722.0	241.50	445.52	6.4268×10^{-3}	21.58	TNEQ
7	12.50	34229	6684.3	234.30	644.52	9.5832×10^{-3}	21.78	TNEQ
8	13.25	32283	6644.9	228.76	863.14	1.3145×10^{-2}	21.91	TNEQ
9	13.95	30480	6596.7	226.91	1127.6	1.7313×10^{-2}	21.84	TNEQ
10	14.75	28236	6527.1	224.73	1568.1	2.4310×10^{-2}	21.71	TNEQ
11	15.50	25772	6428.3	222.35	2256.0	3.5348×10^{-2}	21.50	TNEQ
12	16.25	22949	6286.6	219.47	3520.8	5.5888×10^{-2}	21.17	TNEQ
13	17.00	19790	6091.7	216.65	5705.3	9.1741×10^{-2}	20.64	TNEQ
14	17.75	16355	5836.4	216.65	9723.1	1.5635×10^{-1}	19.77	TNEQ
15	18.25	13962	5631.8	216.65	14170	2.2786×10^{-1}	19.08	TNEQ
16	18.50	12748	5519.6	216.65	17379	2.7946×10^{-1}	18.70	TEQ[b]
17	18.75	11528	5401.2	216.65	20984	3.3743×10^{-1}	18.30	TEQ
18	19.00	10309	5277.1	221.31	25309	3.9840×10^{-1}	17.69	TEQ
19	19.50	7892	5014.3	236.86	36168	5.3196×10^{-1}	16.25	TEQ
20	20.00	5536	4736.5	252.11	50198	6.9366×10^{-1}	14.88	TEQ
21	20.50	3273	4449.6	267.04	67922	8.8610×10^{-1}	13.58	TEQ
22	21.00	1129	4159.7	280.68	88253	1.0954	12.38	TEQ
23	21.28	0	4000.0	288.15	101325	1.2250	11.75	TEQ

[a]Thermal nonequilibrium. [b]Thermal equilibrium.

Table 2 Finite rate reaction chemistry model for 11 species air–carbon[a]

Reaction no.	Reaction	M	T_x	C	η	T_d, K	Reference
1	$N_2 + M <=> N + N + M$	M_{vib}	$\sqrt{T T_{ve}}$	7.0E+21	−1.6	113,200	34,35
		M_{atom}	$\sqrt{T T_{ve}}$	3.0E+22	−1.6	113,200	34,35
2	$O_2 + M <=> O + O + M$	M_{vib}	$\sqrt{T T_{ve}}$	2.0E+21	−1.5	59,500	34,35
		M_{atom}	$\sqrt{T T_{ve}}$	1.0E+22	−1.5	59,500	34,35
3	$NO + M <=> N + O + M$	M_{vib}	$\sqrt{T T_{ve}}$	5.0E+15	0.0	75,500	34,35
		M_{atom}	$\sqrt{T T_{ve}}$	1.1E+17	0.0	75,500	34,35
4	$CO + M <=> C + O + M$	M_{vib}	$\sqrt{T T_{ve}}$	2.3E+20	−1.0	129,000	35
		M_{atom}	$\sqrt{T T_{ve}}$	3.4E+20	−1.0	129,000	35
5	$CO_2 + M <=> CO + O + M$	M_{vib}	$\sqrt{T T_{ve}}$	6.9E+21	−1.5	63,275	35
		M_{atom}	$\sqrt{T T_{ve}}$	1.4E+22	−1.5	63,275	35
6	$CN + M <=> C + N + M$	M_{vib}, M_{atom}	$\sqrt{T T_{ve}}$	2.5E+14	0.0	71,000	35
7	$C_2 + M <=> C + C + M$	M_{vib}, M_{atom}	$\sqrt{T T_{ve}}$	3.7E+14	0.0	69,000	35
8	$C_3 + M <=> C_2 + C + M$	M_{vib}, M_{atom}	$\sqrt{T T_{ve}}$	6.3E+16	−0.5	101,200	13
9	$N_2 + O <=> NO + N$	——	T	6.4E+17	−1.0	38,400	34,35
10	$NO + O <=> O_2 + N$	——	T	8.4E+12	0.0	19,450	34,35
11	$CO + O <=> O_2 + C$	——	T	3.9E+13	−0.18	69,200	35
12	$CO_2 + O <=> O_2 + CO$	——	T	2.1E+13	0.0	27,800	35
13	$CO + C <=> C_2 + O$	——	T	2.0E+17	−1.0	58,000	35
14	$CO + N <=> CN + O$	——	T	1.0E+14	0.0	38,600	35
15	$N_2 + C <=> CN + N$	——	T	1.1E+14	−0.11	23,200	35
16	$CN + O <=> NO + C$	——	T	1.6E+13	0.1	14,600	35
17	$CN + C <=> C_2 + N$	——	T	5.0E+13	0.0	13,000	35

[a] $k_f = C T_x^{\eta} \exp(-T_d / T_x)$, $cm^3/mol \cdot s$, $M_{vib} = N_2$, O_2, NO, CO, CO_2, CN, C_2, C_3, and $M_{atom} =$ N, O, C.

The two-temperature model of Park[34] and Park et al.[35] for nonionizing air consisting of five species (N_2, O_2, NO, N and O) is used. In addition, the following six products of ablation are allowed to enter the flowfield via the surface mass transfer boundary condition and react with the air: CO, CO_2, CN, C_2, C_3, and C. The finite rate reaction chemistry set for these 11 species is composed of 8 dissociation/recombination reactions and 9 exchange reactions. The forward reaction rate coefficients and temperatures used in evaluating the rates are given in Table 2. The backward rates are determined from the equilibrium constants, which are determined from curve fits from the JANNAF tables. The vibrational energy source term is given by the Landau–Teller formula (see Ref. 36) for harmonic oscillators.

The species viscosities for the air species are calculated using the reacting air model of Blottner et al.[37] For the carbon species, coefficients using the Blottner et al. form are from Candler[38] and Olynick et al.[13] and are given in Table 3. The species thermal conductivities are determined through an Eucken relation (see Ref. 36). The total viscosity and conductivity are then calculated using Wilke's semiempirical mixing rule.[39] The species diffusion coefficients are determined by assuming a constant Schmidt number of 0.5 for all species.

For the computations presented in this paper, the flow on the nosetip was assumed to be completely laminar. Although this assumption is not valid late in the trajectory, the primary purpose of this investigation was to develop and evaluate the coupling procedure. Future work will include the effects of turbulent flow.

For all of the trajectory points the freestream Mach number is supersonic, thus allowing the use of a supersonic inflow boundary condition. For the outflow, a zeroth-order extrapolation boundary condition is used because the flow exiting the computational domain is primarily supersonic, except in the small region of the boundary layer near the surface. A symmetry boundary condition is used at the axisymmetric centerline.

For the surface, two boundary conditions are employed. For the initial, nonablating case, a no-slip, isothermal wall is used. In addition, a fully catalytic condition is assumed for the species, allowing full recombination of the dissociated air species. When ablation occurs, however, the boundary condition is altered. The new surface shape and the nodal temperatures are determined by the material thermal response code, and the CFD grid is remeshed for this new surface. At each surface point, the mass flux of ablation products is specified at the wall and allowed to enter the flowfield as blowing normal to the surface. Finally, the mass fractions of the species are based on an equilibrium thermochemical calculation at the surface. This boundary condition is discussed further in later sections.

Table 3 Species viscosity curve fits for 11 species air–carbon model[a]

Species	A_s	B_s	C_s	Reference
N_2	0.0268142	0.3177838	−11.3155513	37
O_2	0.0449290	−0.0826158	−9.2019475	37
NO	0.0436378	−0.0335511	−9.5767430	37
N	0.0115572	0.6031679	−12.4327495	37
O	0.0203144	0.4294404	−11.6031403	37
CO	−0.019527394	1.013295	−13.97873	38
CO_2	−0.019527387	1.047818	−14.32212	38
CN	−0.0083811	0.7860330	−12.9406	13
C_2	−0.0084311	0.7876060	−13.0268	13
C_3	−0.0084312	0.787609	−12.8240	13
C	−0.0083285	0.7703240	−12.7378	13

[a] Here $\mu_s = 0.1 \exp[(A_s \ln T + B_s) \ln T + C_s]$ kg/m · s, T in Kelvin.

Material Thermal Response

The material thermal response for the carbon–carbon nosetip presented in this paper was computed with a modified version of the COYOTE II computer program.[40,41] COYOTE II is a general purpose program designed for the solution of heat conduction problems and other types of diffusion problems and is based on the Galerkin form of the finite element method. COYOTE, in its basic form, contains a large number of features that make it ideal for modeling geometrically complex components. These features include internal heat generation; numerous types of boundary conditions, such as convection, external radiation, and enclosure radiation; and variable material properties that are functions of temperature.

The version of COYOTE used for this work has been modified from the original form. A boundary condition has been developed to allow the position-dependent heat flux computed by the Navier–Stokes code to be applied to the heated surface of the vehicle. The heat flux is applied as the product of a heat transfer coefficient and the difference between the recovery and wall enthalpies. This heating is applied on a node-by-node basis with a direct match between the nodes in the finite volume Navier–Stokes mesh and the Galerkin finite element mesh. This procedure results in a high spatial resolution for the ablating surface without the need to interpolate between meshes.

Additional modifications to the COYOTE code have been made to allow for ablating surfaces and the resultant moving finite element mesh. Two ablation models have been incorporated in the code: a heat of ablation, or Q^* model,[42] and an equilibrium surface

chemistry model. The analyses performed for this paper used the equilibrium chemistry model. For ablating surfaces, the local surface energy balance is written in the form

$$-k\frac{\partial T}{\partial n} = C_h(i_r - i_w) - \varepsilon_w\sigma\left(T_w^4 - T_\infty^4\right) - \dot{m}_c''(i_w - i_c) \qquad (1)$$

where the term on the left side is the heat conduction into the surface of the ablator and the three terms on the right side represent the convective heating, the radiative exchange with the environment, and the energy removed from the surface due to the ablation process, respectively. The convection term is represented as the product of the heat transfer coefficient and the difference between the recovery enthalpy outside the thermal layer and the gas enthalpy at the wall temperature. The ablation term is represented as the product of the ablation mass flux and the difference between the gas enthalpy at the wall temperature and the char enthalpy.

The equilibrium surface chemistry ablation model uses tables of quantities computed by the ACE code.[43] These tables include gas enthalpy i_w and dimensionless ablation mass transfer rate B_c' as functions of pressure and temperature. The quantity B_c' represents the mass flux of ablator removed from the surface per mass of gas arriving at the surface and can be thought of as a dimensionless ablation rate. To compute the ablation mass flux $\dot{m}_c''$, quantity B_c' must be multiplied by a mass transfer coefficient C_m.

The Navier–Stokes solution provides the initial local convective heat transfer rate to the surface q_{conv}. From the wall temperature and pressure, the ACE table is used to determine the gas enthalpy i_w and the dimensionless ablation mass ratio B_c'. With the assumption that the local recovery enthalpy outside the thermal boundary layer i_r equals the freestream stagnation enthalpy, the local heat transfer coefficient C_h can be determined from the definition of the convective heat flux with the equation

$$C_h = q_{\text{conv}}/(i_r - i_w) \qquad (2)$$

Given the assumption that the convective mass transfer coefficient equals the convective heat transfer coefficient, that is,

$$C_m = C_h \qquad (3)$$

the ablation mass flux is determined from the product of the convective mass transfer coefficient and the dimensionless ablation mass ratio, that is,

$$\dot{m}_c'' = C_m B_c' \qquad (4)$$

With the definition of the char enthalpy

$$i_c = \int_{T_{\text{ref}}}^{T} C_p(T)\,\mathrm{d}T + i_{\text{ref}} \qquad (5)$$

all of the quantities on the right-hand side of the surface energy balance are known for a given surface temperature and pressure.

The surface recession and subsequent movement of the surface nodes are computed from the definition of $\dot{m}_c''$ presented. The surface recession rate $\dot{s}$ is computed from the ablation mass flux $\dot{m}_c''$ from the relation

$$\dot{s} = \dot{m}_c''/\rho_c \qquad (6)$$

The surface recession rate is then used to compute the surface nodal displacements over a time step of Δt with the relation

$$\begin{bmatrix}\delta_x\\ \delta_y\end{bmatrix} = \begin{bmatrix}\dot{s}\Delta t n_x\\ \dot{s}\Delta t n_y\end{bmatrix} \qquad (7)$$

where n_x and n_y are the x and y components of the nodal surface inward unit normal $\hat{n}$, respectively.

The ablating surface results in the need to modify the finite element mesh during the solution process. A moving mesh capability was developed and added to COYOTE that is similar to that proposed by Lynch and O'Neill[44] and implemented by Hogan et al.[42] In this method, the mass loss rate per unit area $\dot{m}_c''$ is computed from Eq. (4), and the displacements of the surface nodes are in turn computed from the mass loss rates. These surface displacements are then used as the boundary conditions for a two-dimensional linear elastic solid mechanics model that is used to compute the motion of the interior nodes. This approach is ideal for unstructured grid problems in that it compresses the mesh dependably with little incidence of grid line crossing. For simplicity, planar two-dimensional deformation of a fictitious material is assumed regardless of whether the ablation is planar or axisymmetric. This technique is sufficient because it is simply being used to displace the mesh rather than compute an accurate deformation of a real material.

The equations governing the movement of the mesh are written in terms of nodal displacements as[45]

$$\frac{\partial}{\partial x}\left(c_{11}\frac{\partial \delta_x}{\partial x} + c_{12}\frac{\partial \delta_y}{\partial y}\right) + c_{33}\frac{\partial}{\partial y}\left(\frac{\partial \delta_x}{\partial y} + \frac{\partial \delta_y}{\partial x}\right) = 0 \qquad (8)$$

$$c_{33}\frac{\partial}{\partial x}\left(\frac{\partial \delta_x}{\partial y} + \frac{\partial \delta_y}{\partial x}\right) + \frac{\partial}{\partial y}\left(c_{12}\frac{\partial \delta_x}{\partial x} + c_{22}\frac{\partial \delta_y}{\partial y}\right) = 0 \qquad (9)$$

where the c_{ij} coefficients are dependent on the properties of the fictitious material being deformed and whether a plane strain or plane stress assumption is being employed.[45] For this application, a plane strain formulation was used, with the constant values shown here:

$$c_{11} = c_{22} = c_{12} = 1, \qquad c_{33} = \tfrac{1}{2} \qquad (10)$$

The mesh movement and the in-depth conduction analysis are computed within COYOTE using a segregated approach. Initially the mesh movement for a given COYOTE time step is computed using the temperature field computed for the previous COYOTE time step, the convective heat flux computed by the Navier–Stokes code, and the dimensionless ablation mass ratios. The in-depth conduction problem is then solved using the computed mesh movement and the energy flux terms on the right side of Eq. (1). Although a small amount of accuracy is sacrificed by using this segregated approach, the relatively small time steps used by COYOTE (typically 0.0001–0.01 s for these cases) maintain solution accuracy.

Comparisons have been made between one-dimensional solutions obtained from the CMA code[2] and COYOTE for equilibrium chemistry ablating cases and between the SODDIT code[46] and COYOTE for Q^* ablating cases. In both comparisons, excellent agreement between the codes was obtained. COYOTE was also compared with a one-dimensional analytic Q^* ablation solution, again with excellent agreement.

Iterative Fluid/Thermal Coupling

The original interface between SACCARA and COYOTE, illustrated in Fig. 1, is best described as a loose or explicit coupling between the fluid and thermal response codes.[19] The SACCARA code was run to obtain a steady-state flowfield solution at a trajectory point, providing a convective heating rate, recovery enthalpy, and pressure at each surface node. COYOTE, after computing the heat transfer coefficient from the heat transfer rate, recovery enthalpy, and wall gas enthalpy, then computed the time-dependent material response in a specified time interval between trajectory points, assuming that the heat transfer coefficient, pressure, and recovery enthalpy remained constant at each surface node throughout the interval. The dimensionless ablation rate and pressure for each nodal location were then provided to a version of the ACE code, which computed the injected species mass fractions at the surface. The surface temperatures and ablation rates computed by COYOTE and the blowing species mass fractions computed by ACE were used as the boundary conditions for the SACCARA computations at the next trajectory point. The surface displacements computed by COYOTE were then used to construct the new flowfield grid using

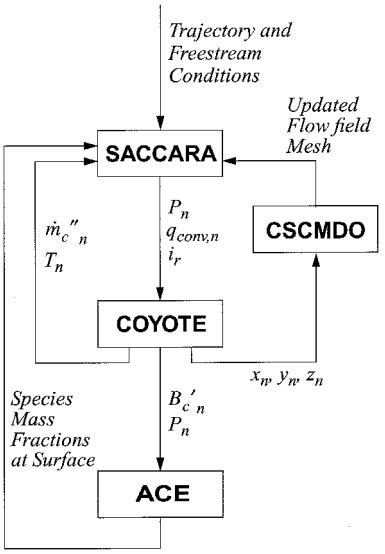

Fig. 1 Original, noniterative fluid/thermal coupling approach.

the code CSCMDO.[47] CSCMDO uses a face deformation approach to move the CFD volume mesh such that it conforms to the new surface while maintaining the grid quality of the original mesh, as long as the original and new surface are in the same parametric form. Implicit in this essentially zeroth-order coupling technique was the assumption that the trajectory points are close enough together that constant heat transfer coefficient, surface pressure, and recovery enthalpy across the time interval produce sufficiently accurate results.

Unfortunately, calculations using this coupling technique (refinements of the calculations reported in Ref. 19) produced large instabilities in calculated surface quantities during the portions of the trajectory in which significant ablation was occurring. These instabilities were the result of the highly nonlinear nature of the ablation process. Small changes in heating rate and surface temperature result in large changes in ablation and surface blowing rate. The large changes in the blowing rate cause significant changes in subsequent heating rates that result in large oscillations in surface heating as the solution technique moves from trajectory point to trajectory point.

To eliminate these oscillations and to improve the accuracy of the coupling technique, an iterative approach was developed. This iterative approach is illustrated in Fig. 2 and contrasted with the earlier approach in Fig. 3. In the noniterative technique, the quantities C_h, P, and i_r, computed by SACCARA at trajectory point n, were held constant within COYOTE as it computed the material thermal response in the interval between trajectory point n and trajectory point $n+1$. In the iterative technique, two SACCARA solutions are employed, one at trajectory point n, and one at trajectory point $n+1$, with COYOTE linearly interpolating in time the quantities C_h, P, and i_r obtained from the two solutions. Initially, the quantities C_h, P, and i_r at trajectory point $n+1$ are obtained from a quadratic extrapolation in time (linear for trajectory point 3 and zeroth order for trajectory point 2) from previous SACCARA solutions. COYOTE is initially run using the SACCARA solution at trajectory point n and the extrapolated quantities to obtain the surface nodal properties at trajectory point $n+1$. SACCARA is then run for trajectory point $n+1$ using these nodal properties to obtain a new set of C_h, P, and i_r values for COYOTE to use in its linear interpolation. This process is repeated until subsequent SACCARA solutions converge on a fixed flowfield solution. The process is then repeated to move from trajectory point $n+1$ to trajectory point $n+2$.

This iterative technique replaces the assumption of constant heat transfer coefficient, surface pressure, and recovery enthalpy between trajectory points with the assumption of linearly varying quantities. This assumption, combined with the iteration with SACCARA solutions, increases the solution accuracy significantly from zeroth order to first order in time at the expense of additional computational time, the vast majority of which is the SACCARA solution time.

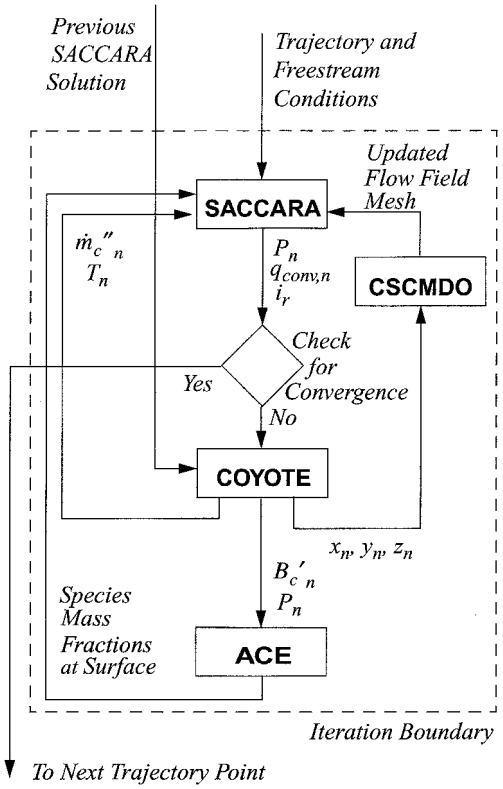

Fig. 2 Iterative fluid/thermal coupling approach.

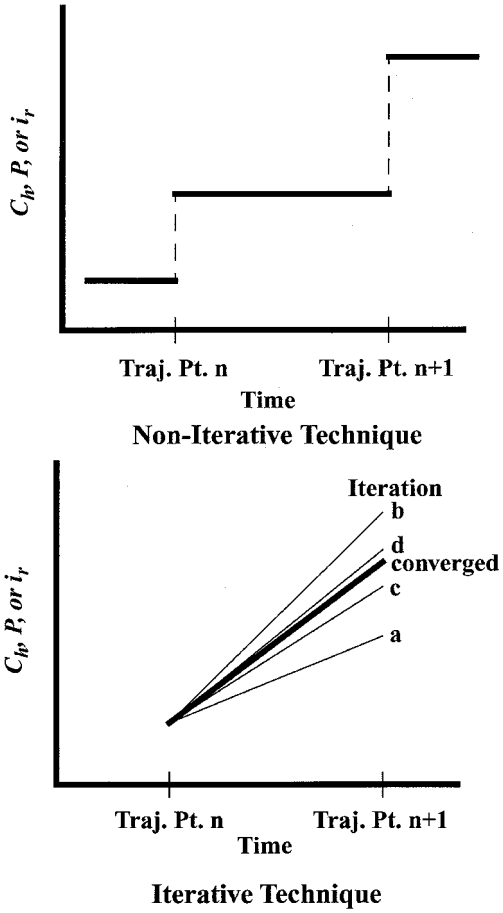

Fig. 3 Comparison of noniterative and iterative fluid/thermal coupling approaches.

Fig. 4 IRV-2 vehicle.

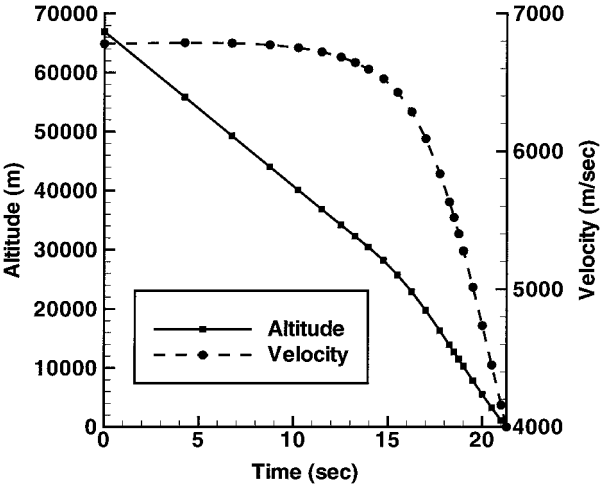

Fig. 5 Trajectory calculation points.

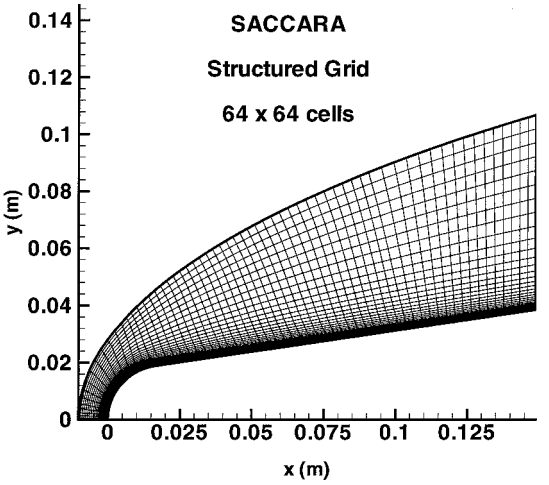

Fig. 6 Initial SACCARA computational grid.

Each SACCARA solution is restarted from the preceding iterative solution to reduce computational expense.

Results

The calculations described in this paper are performed on the nosetip of the IRV-2 vehicle shown in Fig. 4. The IRV-2 vehicle is a sphere–biconic with a nose radius of 0.01905 m (0.75 in.) and total length of 1.386 m (54.56 in.). The biconic angles are 8.42 and 6.10 deg, respectively, with the break occurring at an axial location of 0.1488 m (5.86 in.) measured from the stagnation point. Six drag flaps are located at the aft end of the vehicle and can be deployed to a maximum angle of 45 deg, measured with respect to the vehicle centerline. For this paper, only axisymmetric calculations on the IRV-2 nosetip (sphere and first cone) are made.

The freestream conditions for the simulated trajectory are given in Table 1 and shown graphically in Fig. 5. This trajectory differs from the actual IRV-2 flight trajectory and is somewhat artificial in that it has relatively high velocities through to impact. This type of flight profile was chosen for two reasons. First, the high velocities late in the trajectory result in a significant amount of heating, resulting in a relatively large amount of ablation and, thus, a severe test of the coupled ablation/shape change technique. Second, early computations indicated that if at anytime in the trajectory the recovery enthalpy approached the wall enthalpy, the convective heat transfer coefficient, computed with Eq. (2), could reach unrealistically high values, resulting in an excessive value of the convective mass transfer coefficient and, thus, unrealistically excessive ablation rates. Therefore, the latter part of the trajectory was modified to ensure that the velocities were high enough to keep the recovery enthalpy higher than the wall enthalpy. This behavior will be discussed in greater detail later in this paper.

The initial CFD computational grid is a structured grid that was generated using GRIDGEN[48] Version 13 and is shown in Fig. 6. The grid cell dimensions are 64 (axial) × 64 (radial) with a first cell spacing at the wall of 1.0×10^{-6} m. For the initial CFD calculation, the flowfield conditions are set to freestream values for trajectory point 1 and a constant wall temperature of 294.4 K. For subsequent calculations, the restart solution from the preceding trajectory point is used with the new freestream and wall boundary conditions as initial conditions. For the equilibrium surface chemistry ablation model, the new surface shape, temperature, incoming mass flux, and mass fractions of species are required input surface boundary conditions for the later trajectory points.

The initial material thermal response (MTR) computational grid, shown in Fig. 7, is an unstructured grid (744 elements) and was created using FASTQ.[49] The outer surface of this grid is identical to the body surface in the CFD grid. The boundary conditions used for the MTR analysis included the symmetry boundary condition on the centerline and an adiabatic boundary condition on the nosetip base. The ablating surface boundary condition included the heat

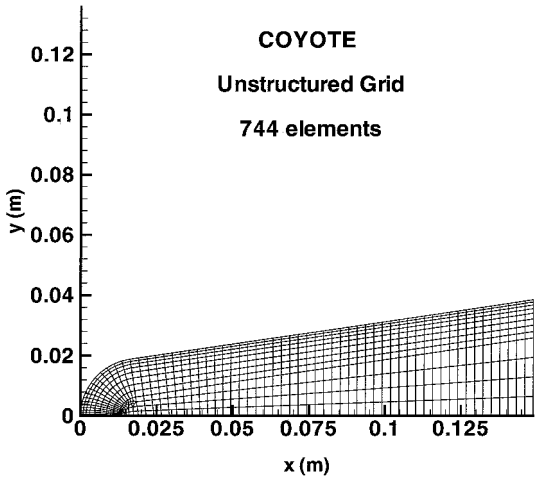

Fig. 7 Initial COYOTE computational grid.

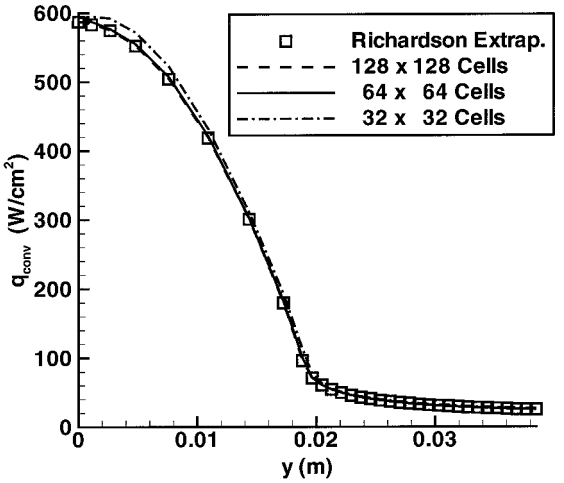

Fig. 8 Effect of grid resolution on convective heating at trajectory point 1.

flux from the SACCARA calculations and radiative exchange with surroundings at a fixed temperature of 190 K.

A grid resolution study was conducted at the first trajectory point to ensure adequate resolution of the boundary layer for the prediction of convective heat transfer. Solutions were produced on two additional grids: 32×32 cells and 128×128 cells. The convective heat flux for the three grids are shown in Fig. 8, along with the solution determined using Richardson extrapolation[50] (RE). The Richardson extrapolated solution, assuming a second-order accurate numerical scheme, is given by the following relationship:

$$q_{\text{conv(RE)}} = q_{\text{conv}(128 \times 128)} + [q_{\text{conv}(128 \times 128)} - q_{\text{conv}(64 \times 64)}]/3 \quad (11)$$

Note that the solutions produced on the 64×64 grid and the 128×128 grid produce nearly identical results, which compare very well with the RE result. Reasonable agreement is also observed with the solution on the coarsest grid. Figure 9 shows a comparison of the relative error between the three solutions as compared with the RE solution. If the mesh has been sufficiently refined where the solution and the error exhibits second-order behavior, then the error in the three solutions should show the following relationship:

$$\%\text{Error in } q_{\text{conv}(128 \times 128)} = [\%\text{Error in } q_{\text{conv}(64 \times 64)}]/4$$
$$= [\%\text{Error in } q_{\text{conv}(32 \times 32)}]/16 \quad (12)$$

By definition, the first equality will be satisfied if Eq. (11) is used for the Richardson extrapolated solution. It is observed that the error for all three solutions less than 0.5% (except at the sphere–cone juncture where it is of order 1.0%). In addition, the largest difference

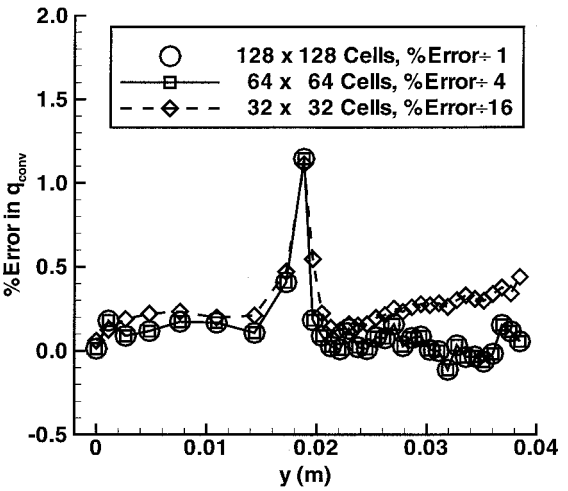

Fig. 9 Solution error in convective heating at trajectory point 1 (as compared to RE).

in the error between the coarsest grid and the two finer grids is of order 0.5%, suggesting that the solutions are near to the asymptotic range. Given the results of this grid convergence study, all further calculations were conducted on the 64×64 grid.

The five to six orders of magnitude reduction of the L_2 norm of the residual on the 64×64 grid required approximately 30,000 iteration steps and 9.75 h of CPU time on a Sun UltraSparc 2 with a 400-MHz processor. Subsequent trajectory points required on the order of 5000–10,000 iteration steps per global iteration because they made use of the solution from the preceding trajectory point or iteration as the initial condition. Improvements in the CPU times and number of iteration steps could have been realized by optimizing the increase of the Courant–Friedrichs–Levy number with an increasing iteration step. CPU times for the thermal calculations varied depending on the time interval solved and the amount of mesh motion that occurs. These CPU times were on the order of minutes and were insignificant when compared to the CFD calculations.

Surface Heat Flux Comparisons

Figure 10 shows the convective heat flux plotted vs the y coordinate for various trajectory points for both the iterative and noniterative techniques. Significant differences in the heating profiles can be seen between the iterative and noniterative techniques, both in the magnitude of the fluxes and in the smoothness of the profiles. The noniterative approach begins to produce wavy profiles as early as trajectory point 5, indicating that instabilities began to form in the solution quite early. The nature of these instabilities is also seen in Fig. 10, where a local maximum in heating rate at one trajectory point results in locally high temperature values and, thus, high blowing rates. The high temperatures and blowing rates, in turn, reduce the calculated convective heating rate at this point on the nosetip at subsequent times in the trajectory, producing the peaks and valleys seen in the heating profiles of Fig. 10. At a trajectory time of approximately 19.0 s (trajectory point 18), the convective heat flux calculated by the noniterative technique became negative, and the computations were terminated.

Results Comparison with ASCC

Computed stagnation point convective heat flux, surface temperature, ablation mass flux, and surface recession are presented in Fig. 11. Included in Fig. 11 are the results of the current iterative calculations, results of the original noniterative calculations, and the results computed with the ASCC.[51] The ASCC is an analytical/correlation-based code for predicting the performance of ablating nosetips. ASCC has been shown to compare very well with flight data for ablating axisymmetric sphere–cones and is considered a good benchmark because it has flight data incorporated into its correlations. The version of ASCC used for this comparison employs the same chemical species as used in the current work.

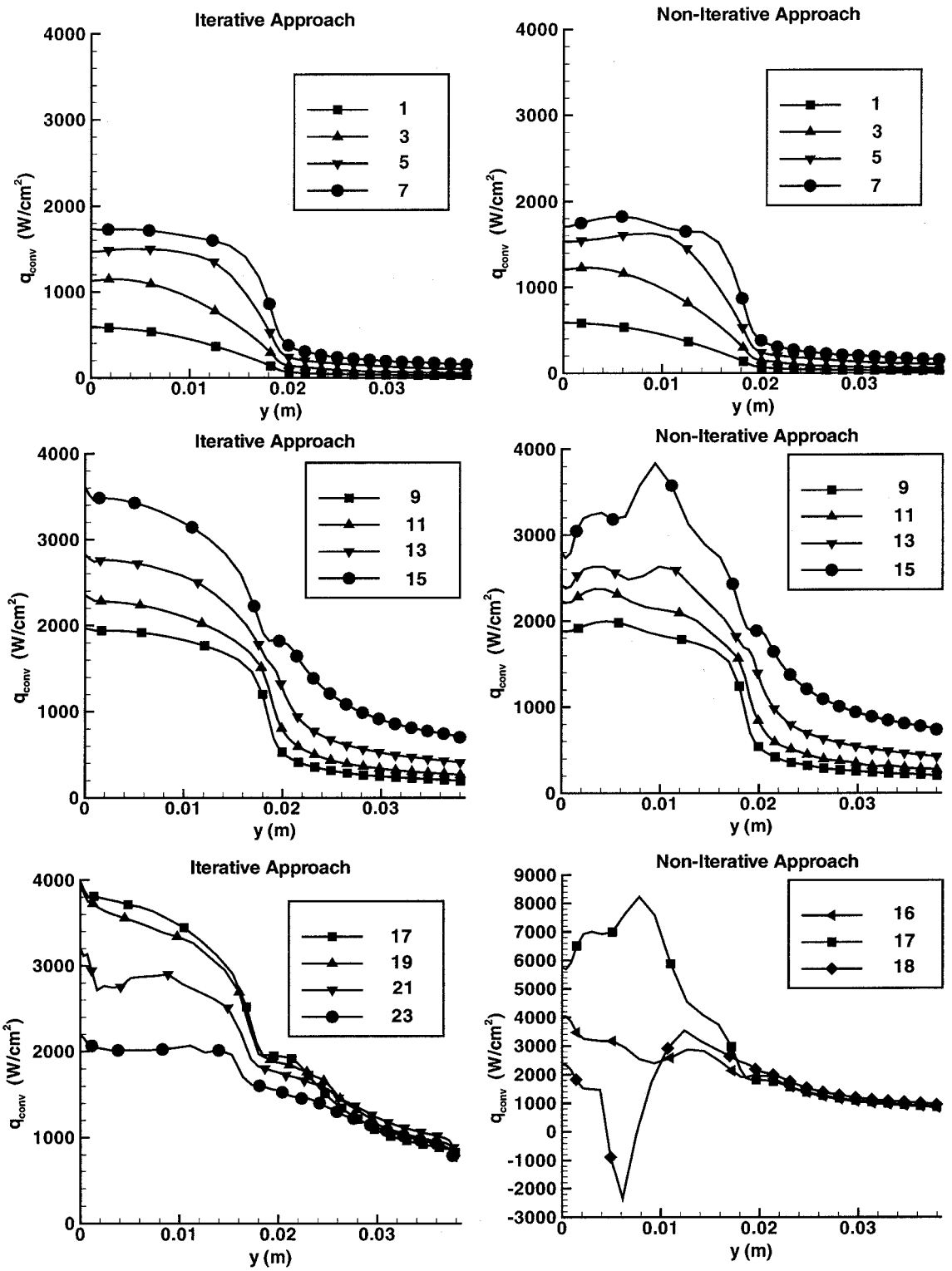

Fig. 10 Heat flux distributions for various trajectory points (indicated in the legends) for the iterative and noniterative approaches.

The agreement between the three techniques is generally good up to a trajectory time of approximately 13 s, when oscillations begin to appear in the noniterative solution technique, as discussed earlier. These oscillations are most apparent in the convective heating rate and the ablation mass flux. The surface temperature and surface recession are relatively insensitive to the computational instabilities. As discussed earlier, the instabilities in the solution appear to have been completely eliminated by the combination of the linear interpolation between SACCARA solutions within COYOTE and the iterative technique that assures agreement between SACCARA and COYOTE from one trajectory point to the next. The relatively good agreement between the iterative solution and the ASCC solution is an indication that the physics of the fluid mechanics and material thermal response are being computed consistently between the two codes.

At approximately 18 s, a significant rise in the convective heating rate and the associated mass flux computed by the iterative technique begins to occur as compared to the ASCC solutions. Both the convective heating rate and the mass flux reach peak values larger than those of the ASCC solution. However, whereas the solutions differ for these two quantities, the surface temperature and, to a lesser extent, the surface recession appear to be fairly insensitive to these

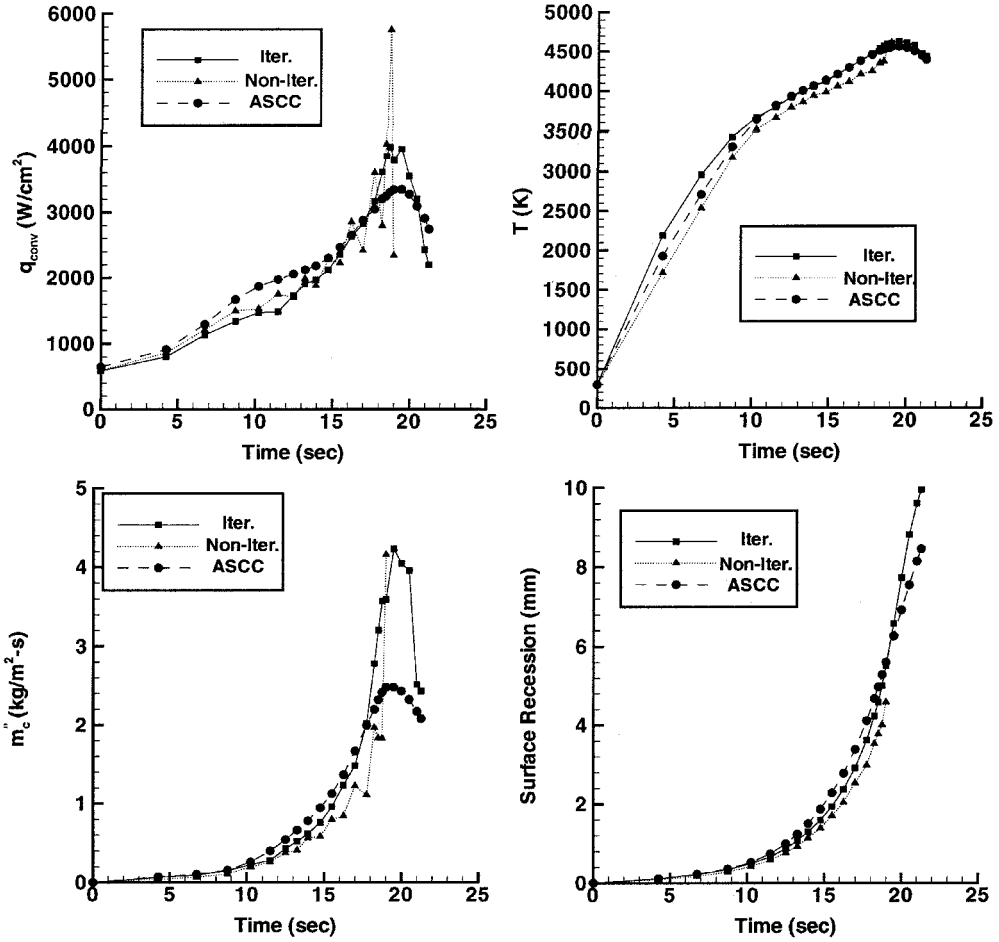

Fig. 11 Stagnation point heat flux, surface temperature, mass flux, and surface recession histories.

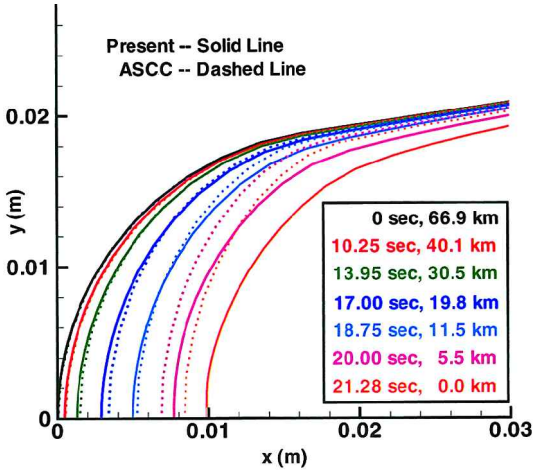

Fig. 12 Ablated surface shape comparison with ASCC.

changes. The difference in peak temperature is only about 60 K. The iterative technique does produce a slightly higher rise in the surface recession, and at impact the iterative technique predicts approximately 1.5 mm more surface recession than the ASCC prediction.

A comparison of the ablated shapes computed with the iterative technique and those computed with the ASCC code during various times in the trajectory is presented in Fig. 12. The agreement between the two techniques is fairly good early in the trajectory and up until about 18.75 s. Early in the trajectory when the heating rates are lower, the relative amount of surface recession is small. However, late in the trajectory the recession begins to increase. Given this recession behavior, it may be possible to decrease the number of trajectory points during the earlier parts of the trajectory where recession is low and then increase the number of points where recession is relatively high.

Near the end of the trajectory, there exist significant differences between the predicted shapes away from the stagnation point. It was observed earlier that the convective heat flux produced by ASCC was lower than the current iterative technique later in the trajectory. ASCC must compute an effective nose radius to compute its heat transfer coefficient. From the shape comparison, it appears that the effective nose radius of the ASCC shapes is larger than that produced by the current iterative technique and, thus, would produce a lower convective heat flux. This could explain some of the differences that we see in the convective heat flux, mass flux, and surface recession, especially late in the trajectory when the relative amount of surface recession is large. Also, ASCC employs correlated pressures and modified Newtonian theory for its inviscid solution that also could be the cause of some of the differences. Given the nature of the assumptions that go into ASCC and the calibrations to flight data, perfect agreement between the two techniques was not expected because the current technique involves a more fundamental approach. However, because ASCC has been shown to compare well with flight data for axisymmetric sphere–cone geometries, its solution is a good benchmark for the present coupled technique.

Iterative Technique Results

The number of iterations needed to converge the global iterations between SACCARA and COYOTE generally ranged from 3 to 5 early in the trajectory to about 20 later in the trajectory when the surface recession is large. The last two trajectory points required about 40 iterations. The number of iterations was dependent on the proximity of the initial extrapolated guess to the final converged solution. Underrelaxation during the iterative process was performed by averaging the solutions from two successive iterations. This

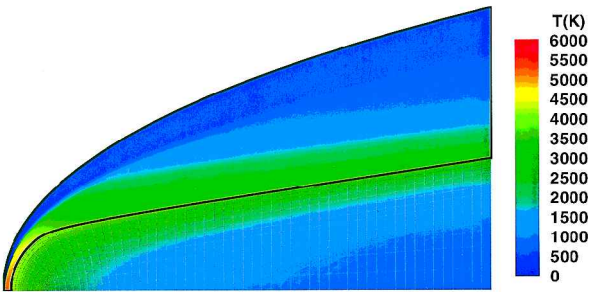

Fig. 13 Flowfield and nosetip temperature contours at impact.

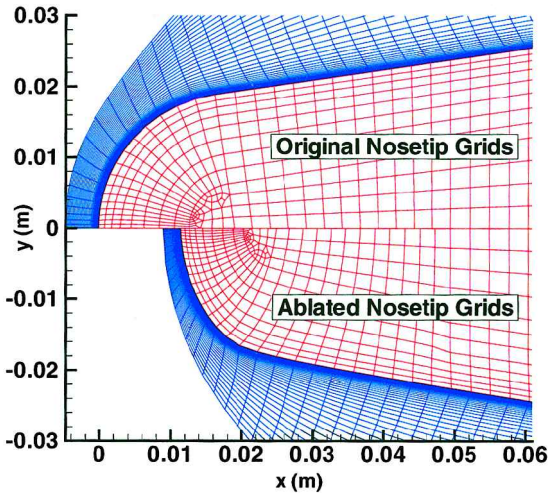

Fig. 14 Original and final numerical meshes.

underrelaxation resulted in an improved iterative convergence behavior because it would damp out any nonphysical peaks or valleys in the computed distributions that are generated in either the extrapolation or iterative processes. The most sensitive variable was the convective heat flux, which directly affects the subsequent ablation mass flux and surface recession. Variables such as surface pressure and temperature converged fairly quickly.

Temperature contours for the flowfield and the solid at impact are presented in Fig. 13. The location of the shock wave, the local high gas temperatures in the vicinity of the spherical nosetip, and the elevated temperatures in the thermal boundary layer along the conical portion of the nosetip are seen in the flowfield portion of Fig. 13. The temperature of the solid, also presented in Fig. 13, shows relatively high temperatures on the spherical portion of the nosetip, where the maximum ablation is occurring. Figure 13 also illustrates the highly two-dimensional nature of the carbon–carbon temperatures. The in-depth temperature variation illustrates the need for multidimensional conduction and the limitation of the more traditional one-dimensional techniques.

Figure 14 compares the CFD and MTR computational grids for initial and final trajectory points. The extent of the nosetip recession at this time in the trajectory and the movement of the CFD and MTR meshes by the CSCMDO and COYOTE codes, respectively, are illustrated in Fig. 14. Although both computational meshes are changed significantly during the trajectory, the quality of the original meshes has been preserved. At impact, almost 10 mm of material has been removed from the nosetip in the stagnation region.

Computational Difficulties

One fundamental difficulty that was encountered dealt with the formulation of the heating/ablation equations. The local heat transfer coefficient C_h is computed from the convective heat flux, the recovery enthalpy, and the wall enthalpy with the relation included earlier as Eq. (2). It is repeated here for convenience:

$$C_h = q_{\text{conv}}/(i_r - i_w) \tag{13}$$

The ablation is computed assuming the mass transfer coefficient is equal to the heat transfer coefficient:

$$C_m = C_h \tag{14}$$

During the initial computations, a trajectory was chosen that included significantly greater deceleration than the one presented in Fig. 5. This trajectory resulted in relatively low velocities late in the flight, such that the value of the wall enthalpy began to approach the value of the recovery enthalpy. This behavior resulted in the denominator of Eq. (13) approaching zero and, thus, the computation of unrealistically high values of the heat and mass transfer coefficients. One possible method to alleviate this situation would be to hold C_h constant at some appropriate value when i_r approaches i_w. Attempts to implement this approach were met with limited success. Thus, the decision was made to reformulate the ablation model with the surface chemistry moved from the COYOTE code to the SACCARA code to eliminate the numerical singularity. For the computations presented in this paper, this situation was avoided by choosing a simulated trajectory with a relatively high impact velocity. This choice prevents the wall enthalpy from approaching the recovery enthalpy and results in realistic values for the heat and mass transfer coefficients throughout the trajectory.

Concluding Remarks

An improved iterative technique to predict the ablation of hypersonic vehicles has been presented. The procedure involves coupling a steady, thermochemical nonequilibrium Navier–Stokes code with an unsteady, multidimensional material thermal response code through mass and energy balances at a common surface interface. Mass in the form of gaseous products of an equilibrium chemistry ablation model is allowed to enter and react with the high-temperature gas flowfield. Surface recession is modeled along the trajectory, which requires readaption of both the fluid and thermal numerical meshes to the receding surface. The iterative technique employed increases the accuracy of the solution technique but does result in additional computational expense. This additional expense may be offset by the need to compute fewer trajectory points.

Results were presented for the ablation of an axisymmetric sphere–cone nosetip for a specified trajectory. The results illustrated the increased robustness of the iterative method over the noniterative method for predicting surface recession over a wide range of thermochemical conditions.

Computed stagnation point surface heat flux, temperature, mass flux, and surface recession were compared to values predicted by the ASCC, and favorable agreement was obtained, indicating that the physics of the fluid mechanics and material thermal response are being computed consistently between the two codes. The predicted ablated shapes compared well between the two techniques until very late in the trajectory where larger differences were seen. Because ASCC has been calibrated with flight data, it provides a good benchmark for the present coupled solution approach.

Acknowledgments

This work was supported the Accelerated Strategic Computing Initiative and Engineering Sciences Research Foundation programs at Sandia National Laboratories. Sandia is a multiprogram laboratory operated by Sandia Corporation, a Lockheed Martin Company, for the U.S. Department of Energy under Contract DE-AC04-94AL85000.

The authors thank David R. Olynick of NASA Ames Research Center and Dean A. Kontinos of Eloret/Thermosciences Institute at NASA Ames Research Center for their helpful discussions on the new iterative coupling approach; Christopher J. Roy of Sandia National Laboratories for his help with the Richardson Extrapolation and grid convergence error calculations; and William T. Jones from the GEOLAB at NASA Langley Research Center for his assistance in implementing and maintaining CSCMDO.

References

[1] Kendall, R. M., Bartlett, E. P., Rindall, R. A., and Moyer, C. B., "An Analysis of the Coupled Chemically Reacting Boundary Layer and Charring Ablator. Part I: Summary Report," NASA CR-1060, June 1968.

[2]Moyer, C. B., and Rindall, R. A., "An Analysis of the Coupled Chemically Reacting Boundary Layer and Charring Ablator. Part II: Finite Difference Solution for the In-Depth Response of Charring Materials Considering Surface Chemical and Energy Balances," NASA CR-1061, June 1968.

[3]Bartlett, E. P., and Kendall, R. M., "An Analysis of the Coupled Chemically Reacting Boundary Layer and Charring Ablator. Part III: Nonsimilar Solution of the Multicomponent Laminar Boundary Layer by an Integral Matrix Method," NASA CR-1062, June 1968.

[4]Bartlett, E. P., Kendall, R. M., and Rindall, R. A., "An Analysis of the Coupled Chemically Reacting Boundary Layer and Charring Ablator. Part IV: A Unified Approximation for Mixture Transport Properties for Multicomponent Boundary-Layer Applications," NASA CR-1063, June 1968.

[5]Kendall, R. M., "An Analysis of the Coupled Chemically Reacting Boundary Layer and Charring Ablator. Part V: Solution of Mixed Equilibrium–Nonequilibrium Homogeneous or Heterogeneous Systems," NASA CR-1064, June 1968.

[6]Rindall, R. A., "An Analysis of the Coupled Chemically Reacting Boundary Layer and Charring Ablator. Part VI: Charring Ablator Response with In-Depth Coking Reactions," NASA CR-1065, June 1968.

[7]Gupta, R. N., Lee, K.-P., Moss, J. N., and Sutton, K., "Viscous-Shock-Layer Solutions with Coupled Radiation and Ablation for Earth Entry," *Journal of Spacecraft and Rockets*, Vol. 29, No. 2, 1992, pp. 173–181.

[8]Henline, W. D., "Thermal Protection Analysis of Mars–Earth Return Vehicles," *Journal of Spacecraft and Rockets*, Vol. 29, No. 2, 1992, pp. 198–207.

[9]Bhutta, B. A., and Lewis, C. H., "New Technique for Low-to-High Altitude Predictions of Ablative Hypersonic Flowfields," *Journal of Spacecraft and Rockets*, Vol. 29, No. 1, 1992, pp. 35–50.

[10]Conti, R. J., MacCormack, R. W., Groener, L. S., and Fryer, J. M., "Practical Navier–Stokes Computation of Axisymmetric Reentry Flowfields with Coupled Ablation and Shape Change," AIAA Paper 92-0752, Jan. 1992.

[11]Chen, Y.-K., and Henline, W. D., "Chemical Nonequilibrium Navier–Stokes Solutions for Hypersonic Flow Over an Ablating Graphite Nosetip," AIAA Paper 93-2836, July 1993.

[12]Chen, Y.-K., Henline, W. D., and Tauber, M. E., "Mars Pathfinder Trajectory Based Heating and Ablation Calculations," *Journal of Spacecraft and Rockets*, Vol. 32, No. 2, 1995, pp. 225–230.

[13]Olynick, D. R., Chen, Y.-K., and Tauber, M. E., "Forebody TPS Sizing with Radiation and Ablation for the Stardust Sample Return Capsule," AIAA Paper 97-2474, June 1997.

[14]Olynick, D. R., Chen, Y.-K., and Tauber, M. E., "Wake Flow Calculations with Ablation for the Stardust Sample Return Capsule," AIAA Paper 97-2477, June 1997.

[15]Bhutta, B. A., Daywitt, J. E., Rahaim, J. J., and Brant, D. N., "New Technique for the Computation of Severe Reentry Environments," AIAA Paper 96-1861, June 1996.

[16]Keenan, J. A., and Candler, G. V., "Simulation of Ablation in Earth Atmospheric Entry," AIAA Paper 93-2789, July 1993.

[17]Keenan, J. A., and Candler, G. V., "Simulation of Graphite Sublimation and Oxidation Under Reentry Conditions," AIAA Paper 94-2083, June 1994.

[18]Chen, Y.-K., and Milos, F. S., "Two-Dimensional Implicit Thermal Response and Ablation Program for Charring Materials on Hypersonic Space Vehicles," AIAA Paper 2000-0206, Jan. 2000.

[19]Hassan, B., Kuntz, D. W., and Potter, D. L., "Coupled Fluid/Thermal Prediction of Ablating Hypersonic Vehicles," AIAA Paper 98-0168, Jan. 1998.

[20]Kuntz, D. W., Hassan, B., and Potter, D. L., "Iterative Approach for Coupling Fluid/Thermal Predictions of Ablating Hypersonic Vehicles," AIAA Paper 99-3460, June 1999.

[21]Kontinos, D. A., "Coupled Thermal Analysis Method with Application to Metallic Thermal Protection Panels," *Journal of Thermophysics and Heat Transfer*, Vol. 11, No. 2, 1997, pp. 173–181.

[22]Wong, C. C., Soetrisno, M., Blottner, F. G., Imlay, S. T., and Payne, J. L., "PINCA: A Scalable Parallel Program for Compressible Gas Dynamics with Nonequilibrium Chemistry," Sandia National Labs., Rept. SAND 94-2436, Albuquerque, NM, April 1995.

[23]Wong, C. C., Blottner, F. G., Payne, J. L., and Soetrisno, M., "Implementation of a Parallel Algorithm for Thermochemical Nonequilibrium Flow Solutions," AIAA Paper 95-0152, Jan. 1995.

[24]"INCA User's Manual," Ver. 2.0, Amtec Engineering, Inc., Bellevue, WA, 1995.

[25]Yoon, S., and Jameson, A., "LU-SSOR Scheme for the Euler and Navier–Stokes Equations," AIAA Paper 87-0600, Jan. 1987.

[26]Yoon, S., and Kwak, D., "Artificial Dissipation Models for Hypersonic External Flow," AIAA Paper 88-3708, June 1988.

[27]Peery, K. M., and Imlay, S. T., "An Efficient Implicit Method for Solving Viscous Multi-Stream Nozzle/Afterbody Flowfields," AIAA Paper 86-1380, June 1986.

[28]Steger, J. L., and Warming, R. F., "Flux Vector Splitting of the Inviscid Gasdynamic Equations with Applications to Finite Difference Methods," *Journal of Computational Physics*, Vol. 40, No. 2, 1981, pp. 263–293.

[29]Yee, H. C., "Implicit and Symmetric Shock Capturing Schemes," NASA TM-89464, May 1987.

[30]Roy, C. J., and Blottner, F. G., "Assessment of One- and Two-Equation Turbulence Models for Hypersonic Transitional Flows," AIAA Paper 2000-0132, Jan. 2000.

[31]Roy, C. J., McWherter-Payne, M. A., and Oberkampf, W. L., "Verification and Validation for Laminar Hypersonic Flowfields," AIAA Paper 2000-2550, June 2000.

[32]Lee, J. H., "Basic Governing Equations for the Flight Regimes of Aeroassisted Orbital Transfer Vehicles," *Thermal Design of Aeroassisted Orbital Transfer Vehicles*, edited by H. F. Nelson, Vol. 96, Progress in Aeronautics and Astronautics, AIAA, New York, 1985, pp. 2–53.

[33]Gnoffo, P. A., Gupta, R. N., and Shinn, J. L., "Conservation Equations and Physical Models for Hypersonic Air Flows in Thermal and Chemical Nonequilibrium," NASA TP-2867, Feb. 1989.

[34]Park, C., "Review of Chemical-Kinetic Problems of Future NASA Missions, I: Earth Entries," *Journal of Thermophysics and Heat Transfer*, Vol. 7, No. 3, 1993, pp. 385–398.

[35]Park, C., Howe, J. T., Jaffe, R. L., and Candler, G. V., "Review of Chemical-Kinetic Problems of Future NASA Missions, II: Mars Entries," *Journal of Thermophysics and Heat Transfer*, Vol. 8, No. 1, 1994, pp. 9–23.

[36]Vincenti, W. G., and Kruger, C. H., Jr., *Introduction to Physical Gas Dynamics*, Krieger, Malabar, FL, 1965, pp. 21, 204.

[37]Blottner, F. G., Johnson, M., and Ellis, M., "Chemically Reacting Gas Viscous Flow Program for Multi-Component Gas Mixtures," Sandia National Labs., Sandia Rept. SC-RR-70-754, Albuquerque, NM, Dec. 1971.

[38]Candler, G. V., "Computation of Thermochemical Nonequilibrium Martian Atmospheric Entry Flows," AIAA Paper 90-1965, June 1990.

[39]Wilke, C. R., "A Viscosity Equation for Gas Mixtures," *Journal of Chemical Physics*, Vol. 18, No. 4, 1950, pp. 517–519.

[40]Gartling, D. K., and Hogan, R. E., "COYOTE II–A Finite Element Computer Program for Nonlinear Heat Conduction Problems, Part I–Theoretical Background," Sandia National Labs., Rept. SAND 94-1173, Albuquerque, NM, Oct. 1994.

[41]Gartling, D. K., and Hogan, R. E., "COYOTE II–A Finite Element Computer Program for Nonlinear Heat Conduction Problems, Part II–User's Manual," Sandia National Labs., Rept. SAND 94-1179, Albuquerque, NM, Oct. 1994.

[42]Hogan, R. E., Blackwell, B. F., and Cochran, R. J., "Application of Moving Grid Control Volume Finite Element Method to Ablation Problems," *Journal of Thermophysics and Heat Transfer*, Vol. 10, No. 2, 1996, pp. 312–319.

[43]Powars, C. A., and Kendall, R. M., "User's Manual–Aerotherm Chemical Equilibrium (ACE) Computer Program," Aerotherm Corp., Mountain View, CA, May 1969.

[44]Lynch, D. R., and O'Neill, K., "Continuously Deforming Finite Elements for the Solution of Parabolic Problems, With and Without Phase Change," *International Journal for Numerical Methods in Engineering*, Vol. 17, No. 1, 1981, pp. 81–96.

[45]Reddy, J. N., *An Introduction to the Finite Element Method*, McGraw–Hill, New York, 1984, p. 266.

[46]Blackwell, B. F., Douglass, R. W., and Wolf, H., "A User's Manual for the Sandia One-Dimensional Direct and Inverse Thermal (SODDIT) Code," Sandia National Labs., Rept. SAND 85-2478, Albuquerque, NM, May 1987.

[47]Jones, W. T., and Samareh-Abolhassani, J., "Grid Generation System for Multidisciplinary Design Optimization," AIAA Paper 95-1689, June 1995.

[48]"GRIDGEN User Manual," Ver. 13, Pointwise, Inc., Bedford, TX, 1998.

[49]Blacker, T. D., "FASTQ Users Manual Version 1.2," Sandia National Labs., Rept. SAND 88-1326, Albuquerque, NM, June 1988.

[50]Roache, P. J., *Verification and Validation in Computational Science and Engineering*, Hermosa, Albuquerque, NM, 1998, pp. 85, 86.

[51]King, H. H. C., Muramoto, K. K., Murray, A. L., and Pronchick, S. W., "ABRES Shape Change Code (ASCC86)—Technical Report and User's Manual," Acurex Corp., Aerotherm Div., Rept. BMO TR-87-57, Mountain View, CA, Dec. 1986.